Light controlled topological plasmonics in a graphene lattice arrayed by metal nanoparticles

Lu Zhang [1] Xi-Ming Wang [1] Xin-Miao Qiu,[1] Zhigang Wang,[2,*] and Jie-Yun Yan [1,3,†]

[1]*School of Science, Beijing University of Posts and Telecommunications, Beijing 100876, China*

[2]*Institute of Applied Physics and Computational Mathematics, Beijing 100088, China*

[3]*State Key Laboratory of Information Photonics and Optical Communications, Beijing University of Posts and Telecommunications, Beijing 100876, China*

The implementation of topology on photonics has opened new functionalities of photonic systems, such as the topologically protected boundary photonic modes. In this study, we investigate topological plasmonics in a graphene lattice arrayed with metal nanoparticles and irradiated by a polarized light. While surface plasmon polaritons are typically excited in such systems, our study shows that the system exhibits a different photonic response with observable edge photonic modes corresponding to distinct topological states. Importantly, we show that the topological phase transition between these states can be easily achieved by controlling the polarization of the external optical field, making it more feasible in experiments than changing the structural parameters. Our system provides a controllable platform for studying topological phenomena in photonics and has potential applications in nanoscale optical devices.

I. INTRODUCTION

The development of topological state theory in condensed matter physics [1–3] has attracted extensive attention. Though insulating in the bulk, these structures support unidirectional and topologically robust edge modes at their boundaries with considerable immunity against backscattering. Because of their special properties, topological insulators have a wide range of potential applications in optical and electrical devices [4–11]. Extension of the concept to photonic systems brings about topological photonics, which uses the topological ideas to design and control the behavior of photons, such as the properties of robust optical transport against defects and disorders, which is not available in the traditional photonic system.

Light-excited arrays of coupled metal nanoparticles (MNPs) are a class of plasmonic systems deeply studied for their extensive applications [12–14], such as the sub-diffraction waveguiding [15], and have become potential candidates for waveguides in dense integrated nanophotonic systems. Nontrivial topology has been previously realized in one-dimensional (1D) plasmonic arrays and quasi-1D zigzag chains [16–19]. These systems, similar to the Su-Schrieffer-Heeger (SSH) [20] model, exhibit highly localized edge states and strong robustness against perturbations. However, since these edge modes are zero dimensional or, say, localized, they cannot deliver the most exciting promise of photonic topological insulators (PTIs), namely, the robust transmission using edge states.

To overcome this limitation, the PTIs beyond one-dimensional (1D) cases are designed and therefore the 2D

plasmonic structures has naturally been paid attentions to. In 2D lattices, the Dirac point [21] is full of vitality in recent studies on topological insulators and topological superconductors. Because the topological properties usually change through the process of band closure and opening, and the Dirac point is just a transition point of closing and opening of energy bands, it plays an important role in topological energy band theory. Graphene is well known to hold Dirac points and has many special physical transport properties such as the anomalous integer quantum Hall effect, *Zitterbewegung*, and Klein paradox due to its linear band structure of a Dirac cone without a band gap [22]. However, the Dirac cones in graphene is fixed at the corners of the Brillouin zone. If we could shift their positions, there would be at least one more freedom added to the system for more exotic topological properties.

In this work, we investigate the 2D PTI in the MNPs-arrayed graphene lattices. To excite the plasmon modes within the MNPs, an AC electric field is required, which is typically generated by irradiating with light. While research has been conducted on plasmonic graphene lattices excited by perpendicular AC electric fields [14], this system is challenging to obtain through optical methods due to the transverse nature of light. Our approach involves irradiating the graphene lattice with perpendicular light, which adds the AC electric field in the lattice plane. The anisotropy caused by the external field transforms the system from a common graphene lattice to a complex one, but can exhibit nontrivial topological properties. The system holds both space inversion and time-reversal symmetries, and therefore the Berry curvature cannot be used to characterize its nontrivial topological nature. Importantly, the topological properties can be controlled by the external field's polarization, providing practical applications in PTIs. Our results confirm the existence of a nontrivial topological

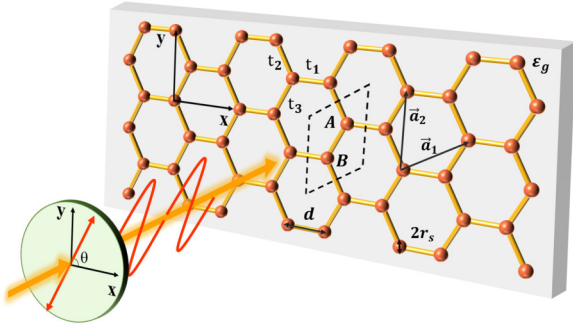*Wang_zhigang@iapcm.ac.cn

†jyyan@bupt.edu.cn

FIG. 1. Schematic representation of the plasmonic lattice consisting of MNPs arranged in a graphene lattice and irradiated perpendicularly by a polarized light. The polarization angle is given relative to the positive direction of the x axis.

phase with zero Berry curvature in 2D plasmonic photonic crystals. We found that this ultracompact plasmonic structure supports one-way topological edge states at its boundaries, allowing light to be guided through arbitrary paths without backscattering. This system's deep subwavelength operation at optical frequencies and simple planar design make it compatible with integrated nanofabrication techniques, enabling the utilization of its exotic photonic topological phases in highly integrated nanophotonic devices.

II. MODEL AND THEORY

The proposed system consists of metal nanoparticles (MNPs) which are arrayed as a two-dimensional graphene lattice, as shown in Fig. 1. Each MNP is modeled as a sphere with the radius of r_s and the nearest-neighbor MNPs are separated by a distance of d with the lattice constant of a. The primitive cell can be constructed by the vectors $\mathbf{a}_1$ and $\mathbf{a}_2$. The lattice is embedded inside the background medium with a permittivity of ε_g. A polarized light is irradiated perpendicularly on the lattice to excite the plasmons within these MNPs. The interaction of the MNPs through the plasmons reshapes the energy distribution in the system, enabling control of the plasmonics by an external field. The polarization direction of the light is a critical factor and the polarization angle is denoted by θ, as shown in Fig. 1.

The plasmonic nanoparticle structure can be accurately modeled using the multipole expansion method [23]. When the condition $r_s/d \leqslant 1/3$ is satisfied, the MNPs can be approximated as point dipoles $\mathbf{p}_i$ that interact through dipolar coupling [24]. In linear and nonmagnetic media, the induced dipole moment $\mathbf{p}_i$ within each MNP is directly proportional to the electric field strength at its position $\mathbf{R}_i$. In the absence of other external excitations, the electric field at each lattice site is the summation of the contributions from all other dipole moments in the array,

$$\mathbf{p}_i = \alpha_E \sum G(\mathbf{R}_i - \mathbf{R}_j)\mathbf{p}_j, \quad (1)$$

where α_E is the polarizability of an individual nanosphere, $\alpha_E = 4\pi\varepsilon_0 r^3[\varepsilon(\omega) - \varepsilon_g]/[\varepsilon(\omega) + 2\varepsilon_g]$. The permittivity of the MNPs $\varepsilon(\omega)$ can be derived by the Drude model $\varepsilon(\omega) = \varepsilon_\infty - \omega_p^2/(\omega^2 + i\omega\gamma)$, where ω_p is the plasma frequency, γ is the damping frequency, and ε_∞ is the permittivity when

frequency goes to infinity. $G(\mathbf{R})$ is the dipole-dipole interaction tensor, $G(\mathbf{r}) = 1/4\pi\varepsilon_0(k^2 + \nabla\nabla)e^{ikr}/r$ [25].

Within each primitive cell, there are two MNPs whose dipole moments can be treated as a pseudospin, denoted as $\mathbf{p}_n = [p_n^1, p_n^2]^T$, located at the position $\mathbf{R}_n$. Since the strength of the dipole-dipole interaction attenuates rapidly with the increasing separation R by $(\propto 1/R^3)$, we only consider the nearest-neighbor coupling. Additionally, we can use the quasistatic approximation because the wavelength of interest is much larger than the lattice constant. As a result, the radiation loss and retardation effect can be ignored. To ensure that the eigenproblem is Hermitian, we do not consider loss in the eigenequation. The vector $\mathbf{p}_n$ must satisfy a self-consistent equation that accounts for the dipole interaction,

$$\frac{1}{\widetilde{\alpha}_E}\mathbf{p}_n = \sum H(\Delta\mathbf{R}_{m,n})\mathbf{p}_m. \quad (2)$$

This is actually an eigenequation: H is the Hamiltonian and $\widetilde{\alpha}_E^{-1} = 4\pi\varepsilon_0/\alpha_E$ is the eigenvalue.

Consider the periodicity of the lattice. The transformed Hamiltonian in momentum space is

$$H(\mathbf{k}) = \begin{pmatrix} 0 & \text{H.c.} \\ t_1 e^{i\mathbf{k}\cdot\mathbf{a_1}} + t_2 e^{i\mathbf{k}\cdot\mathbf{a_2}} + t_3 & 0 \end{pmatrix}, \quad (3)$$

where t_3 and t_1, t_2 are the intracell and intercell interaction strengths between nearest-neighbor MNPs, respectively. By adjusting the polarization, we can change the parameters t_1, t_2, and t_3. For a typical polarization, these parameters cannot be the same at the same time, which means the lattice is no longer the common graphene lattice when irradiated by the external field. The interplay between these three parameters is the key factor in producing the topological phase transition. The evolutions of these three parameters with polarization are plotted in Fig. 2(a), and six special cases are listed in Figs. 2(b)–2(g), where a wider line means a stronger coupling between lattice sites.

To get the energy spectrum, the eigenvalue equation $H(\mathbf{k})\psi(\mathbf{k}) = \widetilde{\alpha}_E^{-1}\psi(\mathbf{k})$ is solved for the optical frequency $\omega(\mathbf{k})$. The Hamiltonian can be represented as a concise form by the Pauli matrix as

$$H(\mathbf{k}) = h(\mathbf{k}) \cdot \sigma. \quad (4)$$

Then the eigenvalue is $\varepsilon_\pm = \pm|h(\mathbf{k})|$. The energy spectrum contains two subbands and is symmetric around zero energy. Eigenvectors for bulk states are obtained as

$$|\psi_\pm(\mathbf{k})\rangle = \frac{1}{\sqrt{2}}\begin{pmatrix} \pm 1 \\ e^{i\phi} \end{pmatrix}, \quad (5)$$

where $\phi = \arg[h(\mathbf{k})]$, $\mathbf{k} = (k_x, k_y)$.

The typical parameters are set as follows in our calculations: the lattice constant $a = 50$ nm, the radius of NP $r_s = 5$ nm. The eigenfrequency is normalized by the Dirac frequency of the NP, $\omega_D = \omega_p/\sqrt{2\varepsilon_g + \varepsilon_\infty}$. We use $\varepsilon_g = 1$ for the background medium. The Drude parameter of gold is taken as $\varepsilon_\infty = 1$, $\omega_p = 2 \times \pi \times 2.07 \times 10^{15}$ rad/s, and $\gamma = 2 \times \pi \times 4.45 \times 10^{12}$ rad/s [26]. Our system is non-Hermitian in a strict sense due to the loss. However, because γ is more than two orders of magnitude smaller than ω_p ($\gamma \ll \omega_p$), all simulated results showed indistinguishable change under a lossless assumption, that is, $\gamma = 0$ is a reasonable assumption.
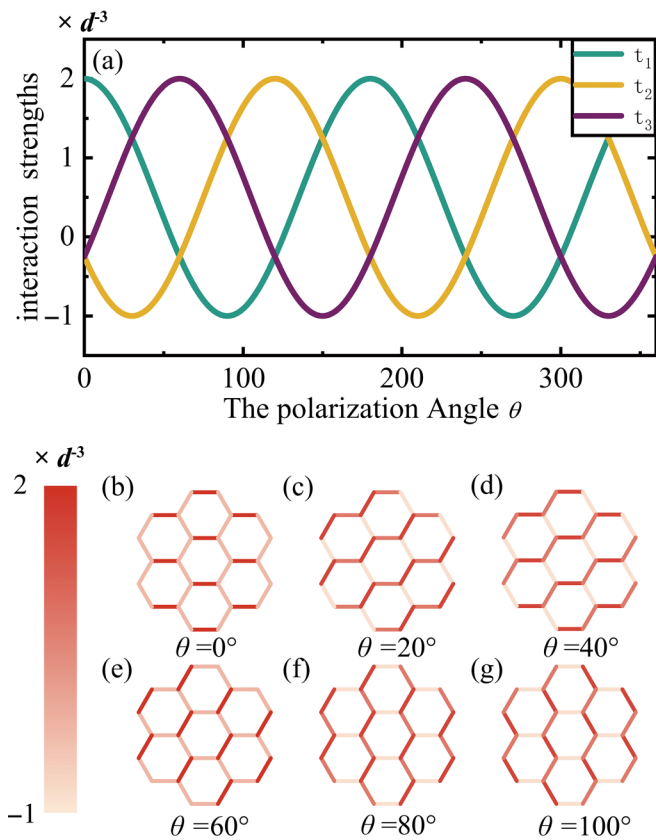
FIG. 2. Evolution of nearest-neighbor hoppings in the nanoparticle lattice as a function of polarization angle. (a) Plots of hopping strengths (t_1, t_2, and t_3) for varying polarization angles. (b) Schematic representation of the lattice structure with nearest-neighbor hopping strengths depicted by the depth of the red color for six selected polarization angles.

The energy spectra are plotted in Figs. 3(a) and 3(b) for two polarization angles, $\theta = 0°$ and $\theta = 30°$, respectively. It is obvious that these two spectra are different from each other: one is gapped and the other is gapless. We explore the spectra for all of the polarization and reach the following conclusion: For the gapped case, the condition $|t_3| < |t_1 \pm t_2|$ (or $|t_3| > |t_1 \pm t_2|$) should be satisfied, where the polarization angle falls in the ranges $\theta = [m60° - 20°, m60° + 20°]$ ($m = 0, 1, \ldots, 5$). The gap disappears when $|t_1 - t_2| < |t_3| < t_1 + t_2$ (or $t_1 + t_2 < |t_3| < |t_1 - t_2|$), which corresponds to the polarization locating within the ranges $\theta = [m60° + 20°, m60° + 40°]$ ($m = 0, 1, \ldots, 5$). All of these are summarized in Fig. 3(c). It should be noted that the mechanism of the band gap formation here is different from the Bragg interference in wavelength-scale photonic crystals, but relies on the resonance of individual nanoparticles. Similar low-frequency band gaps in deep subwavelength resonant electromagnetic or acoustic metamaterials have been previously reported in the literature [27,28], in which the band gap frequency is determined by the resonance frequency of an individual resonator, instead of the specific arrangement of the resonators in the array.

The case of a graphene lattice by a perpendicular excitation has been researched, i.e., all the excited dipoles are along the perpendicular direction of the lattice plane. In that case, the condition $t_1 = t_2 = t_3$ meets and the energy spectrum is just like that of graphene with the Dirac points locating at the corners of the first Brillouin zone. However, introducing the in-plane polarization as we do, the situation becomes complex. The condition $t_1 = t_2 = t_3$ cannot be satisfied, but there still exist two Dirac points when $|t_1 - t_2| < |t_3| < t_1 + t_2$ (or $t_1 + t_2 < |t_3| < |t_1 - t_2|$), as mentioned before. The positions of these Dirac points can be solved analytically as $\mathbf{k} = \pm\mathbf{k}_D$,
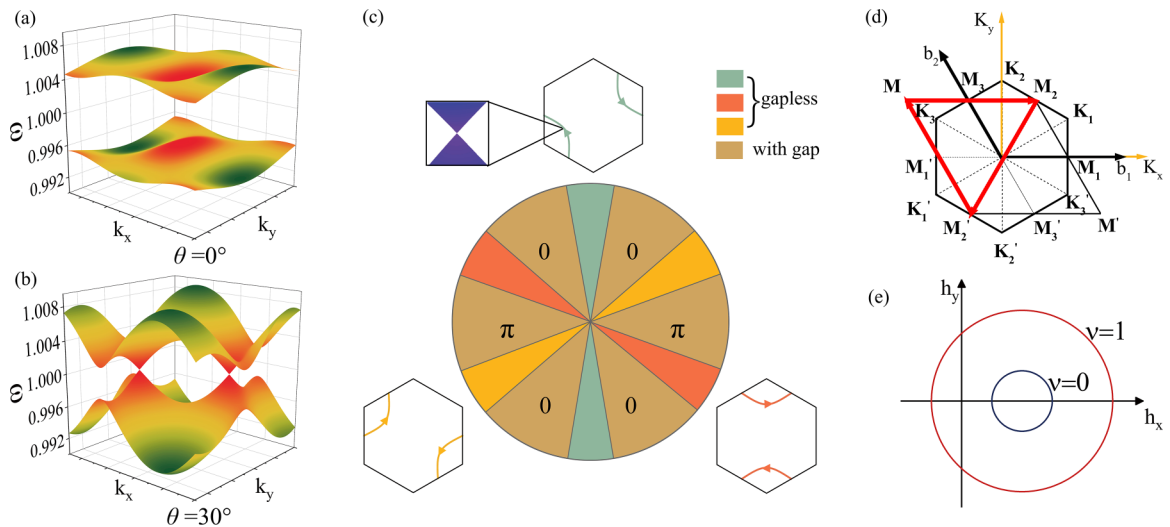

FIG. 3. The energy band structure and topological invariants of the graphene lattice under perpendicular polarized light. (a),(b) Typical gapped and gapless band structures, respectively. (c) The range of polarization angles. The gapless cases are shown in areas without numbers, where the pair of Dirac points moves in the Brillouin zone as indicated by the arrowed curves. The numbered areas represent ranges of polarization angles allowing for gapped cases, with the number indicating the topological invariant or phase gathered around half of the Brillouin zone enclosed by the red lines in (d). (e) The end of vector $\mathbf{h}(k)$ as k varies from 0 to 2π. The winding number is connected to the topological invariant.

with

$$\mathbf{k}_D = \begin{pmatrix} \frac{2}{\sqrt{3}a}\,\mathrm{sgn}(t_3 - t_2)\arccos\left(-\frac{t_2+t_3}{t_1}\sqrt{\frac{t_1^2-(t_2-t_3)^2}{4t_2t_3}}\right) \\ \frac{2}{a}\arccos\left(\sqrt{\frac{t_1^2-(t_2-t_3)^2}{4t_2t_3}}\right) \end{pmatrix}. \quad (6)$$

In Fig. 3(c), we have plotted the traces of two Dirac points in momentum space with arrowed curves in the same colors as the areas where the band gap closes. We observe that these two Dirac points appear in a symmetric position around the Γ point when the parameters permit it. Furthermore, the locations of the Dirac points are not fixed, but evolve with the parameters. This behavior is very different from classical topological phase transition models, such as the famous SSH model, where the band closing and reopening happen at a particular parameter condition to fulfill the topological phase transition. In our system, there is a parameter range rather than a point from one gapped phase to another. Therefore, our next task is to determine whether the band closing and reopening are accompanied by any kind of topological phase transition.

III. TOPOLOGICAL INVARIANT

To topologically differentiate these states when polarization changes, we need to find a topological invariant. Unfortunately, the usually used Berry curvature vanishes in the system due to the existence of both inversion and time-reversal symmetries [29,30]. Nevertheless, the topological properties can still be characterized in terms of the Berry phase in such 2D system, which may be nontrivial even for vanished Berry curvature. Recent studies have shown that topologically nontrivial electronic band structures can emerge even though the Berry curvature is zero, such as in the square lattice [29,31], T-graphene lattice [32], and hexagonal Floquet system [33]. The topological state is characterized by an integration of the Berry connection over the momentum space, the magnetic vector potential whose curl gives the Berry curvature [30], resulting in a nontrivial Zaks phase.

For better analysis, we rewrite the Hamiltonian as

$$H_{\mathbf{k}} = \begin{pmatrix} 0 & \mathbf{h}^*(\mathbf{k}) \\ \mathbf{h}(\mathbf{k}) & 0 \end{pmatrix}, \quad (7)$$

where

$$\mathbf{h}(\mathbf{k}) = h_x(\mathbf{k}) + i h_y(\mathbf{k}), \quad (8)$$

$$h_x(\mathbf{k}) = t_3 + t_1\cos(\mathbf{k}\cdot\mathbf{a_1}) + t_2\cos(\mathbf{k}\cdot\mathbf{a_2}), \quad (9)$$

$$h_y(\mathbf{k}) = t_1\sin(\mathbf{k}\cdot\mathbf{a_1}) + t_2\sin(\mathbf{k}\cdot\mathbf{a_2}). \quad (10)$$

The Berry connection is then $A_i = i\langle\psi|\partial k_i|\psi\rangle$ $(i = x, y)$, and the 2D Berry phase is defined as the line integration around a certain zone. The Berry phase around the whole Brillouin zone (BZ) is zero. But if we turn to the contribution from each half BZ, the underlying mechanism may be clear. The BZ of the lattice is drawn in Fig. 3(d), where the hexagonal BZ is equivalent to that enclosed by the parallelogram. We calculate the Berry phase enclosed by the arrowed red lines in Fig. 3(d),

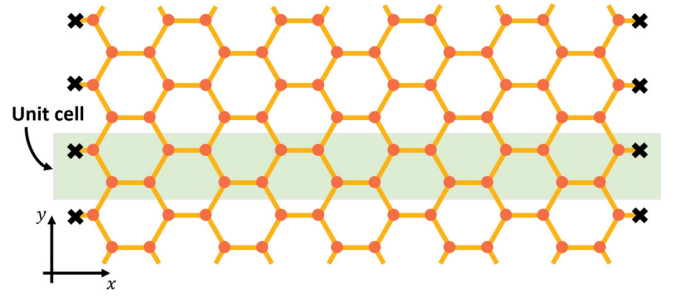$$\gamma = \oint_{L_1} \mathbf{A}(\mathbf{k})d\mathbf{k}. \quad (11)$$

FIG. 4. The nanoribbon obtained by cutting the plasmonic graphene lattice. The nanoribbon is infinite along the y direction and has zigzag edges in the x direction. The shaded area represents a unit cell for the nanoribbon.

The Berry phase of this half BZ can be related to the winding number of the eigenvectors $h(\mathbf{k})$ by the relationship

$$\gamma = \frac{1}{2}\sum\Delta\phi_i(k_i) \quad (i = x, y). \quad (12)$$

The winding number is defined as

$$\nu = \frac{1}{2\pi i}\int_{-\pi}^{\pi} dk\,\frac{d}{dk}\ln[\mathbf{h}(k)], \quad (13)$$

where $\mathbf{h}(k) = v + we^{ik}$. If the end of the vector $\mathbf{h}(k)$ cannot enclose the origin of the complex plane as k goes from 0 to 2π, then ν is zero. On the contrary, if the end encircles the origin once, we can get a nontrivial value of $\nu = 1$, and so on, as shown in Fig. 3(e). The change of the winding number means the topological phase transition. The numerical results are drawn in Fig. 3(c). It is seen that for all those polarizations causing the gapped band structure, the Berry phase gathered around the half part of the BZ is either zero or π. The nonzero Berry phase obtained in this way means the contributions from this and that half parts of the BZ are different, which means an uneven Berry phase distribution. This is the topological invariant chosen by us to describe the different topological phases in the system.

IV. EDGE STATES

One essential feature of the 2D system in nontrivial topological phases is the existence of topological edge states in the corresponding 1D case. We will demonstrate the feature in our system. The 1D case is chosen as a nanoribbon with the width of 20 unit cells along the x direction and with periodic boundary assumption along the y direction, as shown in Fig. 4. It is actually a zigzag graphene nanoribbon if the differences among t_1, t_2, and t_3 are neglected. Numerical results show that when $\theta \sim 0°$–$20°$ (or $\sim 160°$–$180°$), edge states appear in the energy spectrum, as shown in Fig. 5(a) where a typical polarization $\theta = 10°$ is chosen. In contrast, when $\theta \sim 40°$–$80°$ (or $\sim 100°$–$140°$), there are no edge states, as shown in Fig. 5(b) where a typical polarization $\theta = 120°$ is used. The results are consistent with the analytical analysis in the last section.

By solving the eigenproblem, we can determine the dipole moments of all the MNPs and obtain the corresponding electric field distribution. Figure 5(c) shows the field distribution
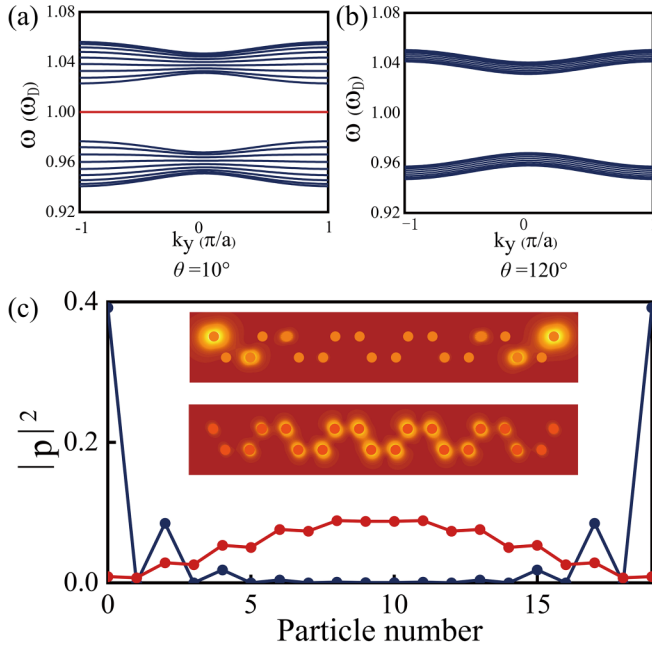
FIG. 5. Projected bulk states and edge states of a plasmonic nanoribbon with 20 sites aligned along the x axis for two polarization angles: (a) $\theta = 10°$ and (b) $\theta = 120°$. The red line in (a) indicates the edge state that appears. (c) The distributions of $|p_i|^2$ in a unit cell for the in-plane polarized edge modes, where the blue (red) line corresponds to $\theta = 10°$ ($\theta = 120°$) with $k_y = 0$. Insets show the normalized electric field distributions in a unit cell caused by these dipoles for each case.

for polarizations of $10°$ and $120°$, respectively, which correspond to two topologically distinct states with completely different energy distributions. Switching between these two states can be achieved by simply adjusting the polarization of the external field, making it a practical method. The ability to control topological states in photonics has generated significant interest due to its potential application in the design of all-optical topological photonics.

V. THE DIPOLE RESPONSE

A classical method to calculate the dipole response to an external polarized field is developed here as an independent way to check the validity of the eigenequation. There is a dipole excitation inside each MNP when the plasmons are excited out by the external electric field. For each MNP, the strength of its dipole is determined by the total electric field at its position, which includes the contributions from all other dipoles inside other MNPs. Therefore, we can obtain the dipole response in a consistent way with the help of classical electromagnetic theory.

We assume that all the MNPs have the same size. Since the parameters of r_s and d are 5 nm and $50/\sqrt{3}$ nm, respectively, the long-wave approximation is still valid. The electric field generated by a single dipole $\mathbf{p}$ is

$$\mathbf{E} = \frac{1}{4\pi\varepsilon_0}\left[\frac{3(\mathbf{p}\cdot\mathbf{r})\mathbf{r}}{r^5} - \frac{\mathbf{p}}{r^3}\right]. \quad (14)$$

Summing up all the contributions from other MNPs, we can obtain the electric field at the position of any MNP, which should comply with the induced dipole inside this MNP. For instance, the electric field at the position of site A in the primary cell numbered (0,0), denoted as $\mathbf{E}_{A_{0,0}}$, includes the contributions from all A-MNPs $\mathbf{E}_{AA_{0,0}}$ and that from all B-MNPs $\mathbf{E}_{BA_{0,0}}$. (n, m) is the position of primary cell, in which there are two sites A and B, as illustrated in Fig. 1. For the two-dimensional problem, it is convenient to decompose each dipole and the electric field into x and y components. Therefore, the electric field at $A_{0,0}$ generated by other MNPs has four contributions:

$$\mathbf{E}_{BA_{0,0}}^{(x)} = \frac{1}{4\pi\varepsilon_0}\sum_{m=-\infty}^{\infty}\sum_{n=-\infty}^{\infty}\left[\frac{3p_{B_x}vd_1(x)^2}{[vd_1(x)^2 + vd_1(y)^2]^{\frac{5}{2}}}\right.$$
$$\left. - \frac{p_{B_x}}{[vd_1(x)^2 + vd_1(y)^2]^{\frac{3}{2}}}\right]\hat{\mathbf{x}}, \quad (15)$$

$$\mathbf{E}_{AA_{0,0}}^{(x)} = \frac{1}{4\pi\varepsilon_0}\sum_{m=-\infty}^{\infty}\sum_{n=-\infty}^{\infty}\left[\frac{3p_{A_x}vd_2(x)}{[vd_2(x)^2 + vd_2(y)^2]^{\frac{5}{2}}}\right.$$
$$\left. - \frac{p_{A_x}}{[vd_2(x)^2 + vd_2(y)^2]^{\frac{3}{2}}}\right]\hat{\mathbf{x}}, \quad (16)$$

$$\mathbf{E}_{BA_{0,0}}^{(y)} = \frac{1}{4\pi\varepsilon_0}\sum_{m=-\infty}^{\infty}\sum_{n=-\infty}^{\infty}\left[\frac{3p_{B_y}vd_1(y)^2}{[vd_1(x)^2 + vd_1(y)^2]^{\frac{5}{2}}}\right.$$
$$\left. - \frac{p_{B_y}}{[vd_1(x)^2 + vd_1(y)^2]^{\frac{3}{2}}}\right]\hat{\mathbf{y}}, \quad (17)$$

$$\mathbf{E}_{AA_{0,0}}^{(y)} = \sum_{m=-\infty}^{\infty}\sum_{n=-\infty}^{\infty}\frac{1}{4\pi\varepsilon_0}\left[\frac{3p_{A_y}vd_2(y)^2}{[vd_2(x)^2 + vd_2(y)^2]^{\frac{5}{2}}}\right.$$
$$\left. - \frac{p_{A_y}}{[vd_2(x)^2 + vd_2(y)^2]^{\frac{3}{2}}}\right]\hat{\mathbf{y}}, \quad (18)$$

where

$$vd_1 = \frac{1-3m}{2}d\hat{\mathbf{x}} + \frac{\sqrt{3}(1-m-2n)}{2}d\hat{\mathbf{y}}, \quad (19)$$

$$vd_2 = \frac{-3m}{2}d\hat{\mathbf{x}} + \frac{\sqrt{3}(-m-2n)}{2}d\hat{\mathbf{y}}, \quad (20)$$

$$vd_3 = \frac{-1-3m}{2}d\hat{\mathbf{x}} + \frac{\sqrt{3}(-1-m-2n)}{2}d\hat{\mathbf{y}}. \quad (21)$$

Similarly, we get

$$\mathbf{E}_{AB_{0,0}}^{(x)} = \frac{1}{4\pi\varepsilon_0}\sum_{m=-\infty}^{\infty}\sum_{n=-\infty}^{\infty}\left[\frac{3p_{A_x}vd_3(x)}{[vd_3(x)^2 + vd_3(y)^2]^{\frac{5}{2}}}\right.$$
$$\left. - \frac{p_{A_x}}{[vd_3(x)^2 + vd_3(y)^2]^{\frac{3}{2}}}\right]\hat{\mathbf{x}}, \quad (22)$$

$$\mathbf{E}_{BB_{0,0}}^{(x)} = \sum_{m=-\infty}^{\infty}\sum_{n=-\infty}^{\infty}\frac{1}{4\pi\varepsilon_0}\left[\frac{3p_{B_x}vd_2(x)^2}{[vd_2(x)^2 + vd_2(y)^2]^{\frac{5}{2}}}\right.$$
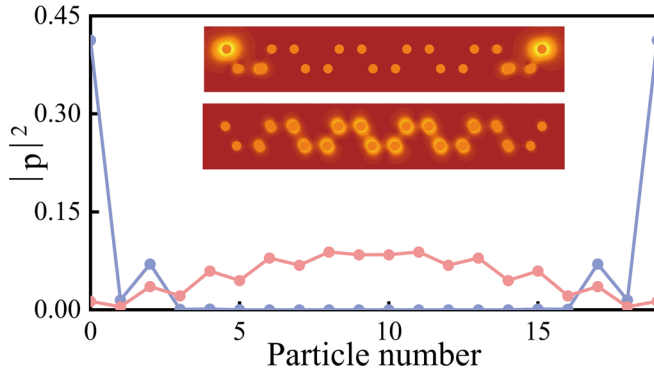$$\left. - \frac{p_{B_x}}{[vd_2(x)^2 + vd_2(y)^2]^{\frac{3}{2}}}\right]\hat{\mathbf{x}}, \quad (23)$$

FIG. 6. The distributions of $|p_i|^2$ within a unit cell for the in-plane polarized edge modes in the lattice of 20-nanosphere width in the x direction. The blue (red) line corresponds to the polarization $\theta = 10°$ ($\theta = 120°$). Inset: The normalized electric field distribution in the unit cell.

$$\mathbf{E}_{AB_{0,0}}^{(y)} = \frac{1}{4\pi\varepsilon_0} \sum_{m=-\infty}^{\infty} \sum_{n=-\infty}^{\infty} \left[\frac{3p_{A_y} v d_3(y)}{[vd_3(x)^2 + vd_3(y)^2]^{\frac{5}{2}}} \right.$$
$$\left. - \frac{p_{A_y}}{[vd_3(x)^2 + vd_3(y)^2]^{\frac{3}{2}}} \right] \hat{\mathbf{y}}, \tag{24}$$

$$\mathbf{E}_{BB_{0,0}}^{(y)} = \sum_{m=-\infty}^{\infty} \sum_{n=-\infty}^{\infty} \frac{1}{4\pi\varepsilon_0} \left[\frac{3p_{B_y} v d_2(y)^2}{[vd_2(x)^2 + vd_2(y)^2]^{\frac{5}{2}}} \right.$$
$$\left. - \frac{p_{B_y}}{[vd_2(x)^2 + vd_2(y)^2]^{\frac{3}{2}}} \right] \hat{\mathbf{y}}. \tag{25}$$

Adding all these parts, we get the field $\mathbf{E}_{A_{0,0}}$,

$$\mathbf{E}_{A_{0,0}}^{(x)} = \mathbf{E}^{(x)} + \mathbf{E}_{BA_{0,0}}^{(x)} + \mathbf{E}_{AA_{0,0}}^{(x)}, \tag{26}$$

$$\mathbf{E}_{A_{0,0}}^{(y)} = \mathbf{E}^{(y)} + \mathbf{E}_{BA_{0,0}}^{(y)} + \mathbf{E}_{AA_{0,0}(y)}^{(y)}. \tag{27}$$

Then, the induced dipole of the $A_{0,0}$ MNP should satisfy the relation

$$\mathbf{p}_{A_{0,0}} = 4\pi r^3 \varepsilon_0 \alpha \mathbf{E}_{A_{0,0}}. \tag{28}$$

The electric field at the MNP $B_{0,0}$ is

$$\mathbf{E}_{B_{0,0}}^{(x)} = \mathbf{E}^{(x)} + \mathbf{E}_{AB_{0,0}}^{(x)} + \mathbf{E}_{BB_{0,0}}^{(x)}, \tag{29}$$

$$\mathbf{E}_{B_{0,0}}^{(y)} = \mathbf{E}^{(y)} + \mathbf{E}_{AB_{0,0}}^{(y)} + \mathbf{E}_{BB_{0,0}}^{(y)}. \tag{30}$$

Finally, we can express all these dipoles by the following equations:

$$\frac{p_{A_x}}{4\pi r_s^3 \varepsilon_0 \alpha_A} = E_x + \frac{1}{4\pi\varepsilon_0} \sum_{m=-\infty}^{\infty} \sum_{n=-\infty}^{\infty} \left[\frac{3v d_1(x)^2}{[vd_1(x)^2 + vd_1(y)^2]^{\frac{5}{2}}} \right.$$
$$\left. - \frac{1}{[vd_1(x)^2 + vd_1(y)^2]^{\frac{3}{2}}} \right] p_{B_x}$$
$$+ \frac{1}{4\pi\varepsilon_0} \sum_{m=-\infty}^{\infty} \sum_{n=-\infty}^{\infty} \left[\frac{3v d_2(x)^2}{[vd_2(x)^2 + vd_2(y)^2]^{\frac{5}{2}}} \right.$$
$$\left. - \frac{1}{[vd_2(x)^2 + vd_2(y)^2]^{\frac{3}{2}}} \right] p_{A_x}; \tag{31}$$
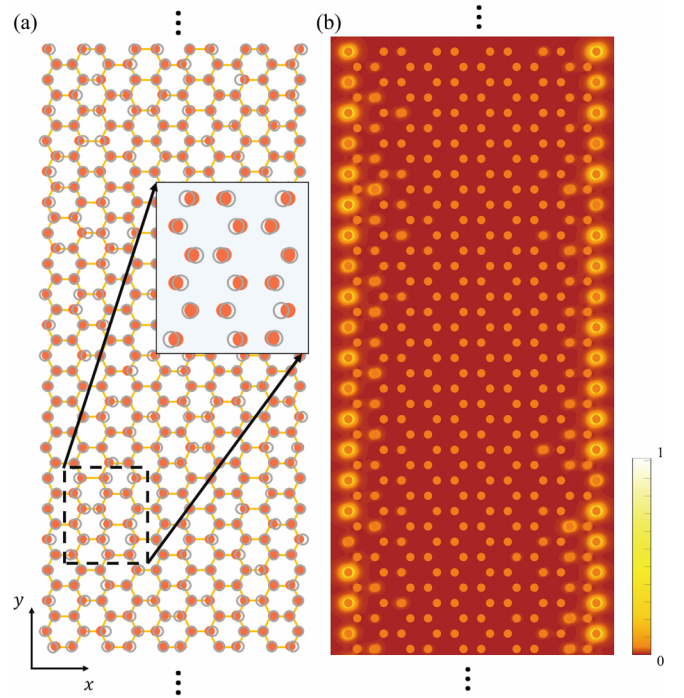

FIG. 7. Check of the robustness of the edge state against the position disorder. (a) The introduced disorder in the lattice with a width of 20 nanospheres in the x direction and 40 nanospheres along the y direction. Only a section in the y direction of the nanoribbon is drawn. The enlarged part shows the offsets of position, where the hollowed circles are the real positions after the disorder is introduced. (b) The field distribution in the disordered lattice.

$$\frac{p_{B_x}}{4\pi r_s^3 \varepsilon_0 \alpha_B} = E_{(x)} + \frac{1}{4\pi\varepsilon_0} \sum_{m=-\infty}^{\infty} \sum_{n=-\infty}^{\infty} \left[\frac{3v d_3(x)^2}{[vd_3(x)^2 + vd_3(y)^2]^{\frac{5}{2}}} \right.$$
$$\left. - \frac{1}{[vd_3(x)^2 + vd_3(y)^2]^{\frac{3}{2}}} \right] p_{A_x}$$
$$+ \frac{1}{4\pi\varepsilon_0} \sum_{m=-\infty}^{\infty} \sum_{n=-\infty}^{\infty} \left[\frac{3v d_2(x)^2}{[vd_2(x)^2 + vd_2(y)^2]^{\frac{5}{2}}} \right.$$
$$\left. - \frac{1}{[vd_2(x)^2 + vd_2(y)^2]^{\frac{3}{2}}} \right] p_{B_x}; \tag{32}$$

$$\frac{p_{A_y}}{4\pi r_s^3 \varepsilon_0 \alpha_A} = E_{(y)} + \frac{1}{4\pi\varepsilon_0} \sum_{m=-\infty}^{\infty} \sum_{n=-\infty}^{\infty} \left[\frac{3v d_1(y)^2}{[vd_1(x)^2 + vd_1(y)^2]^{\frac{5}{2}}} \right.$$
$$\left. - \frac{1}{[vd_1(x)^2 + vd_1(y)^2]^{\frac{3}{2}}} \right] p_{B_y}$$
$$+ \sum_{m=-\infty}^{\infty} \sum_{n=-\infty}^{\infty} \frac{1}{4\pi\varepsilon_0} \left[\frac{3v d_2(y)^2}{[vd_2(x)^2 + vd_2(y)^2]^{\frac{5}{2}}} \right.$$
$$\left. - \frac{1}{[vd_2(x)^2 + vd_2(y)^2]^{\frac{3}{2}}} \right] p_{A_y}; \tag{33}$$

$$\frac{p_{B_y}}{4\pi r_s^3 \varepsilon_0 \alpha_B} = E_{(y)} + \sum_{m=-\infty}^{\infty} \sum_{n=-\infty}^{\infty} \frac{1}{4\pi\varepsilon_0} \left[\frac{3v d_3(y)^2}{[vd_3(x)^2 + vd_3(y)^2]^{\frac{5}{2}}} \right.$$
$$\left. - \frac{1}{[vd_3(x)^2 + vd_3(y)^2]^{\frac{3}{2}}} \right] p_{A_y}$$

$$+ \sum_{m=-\infty}^{\infty} \sum_{n=-\infty}^{\infty} \frac{1}{4\pi\varepsilon_0} \left[\frac{3vd_2(y)^2}{[vd_2(x)^2 + vd_2(y)^2]^{\frac{5}{2}}} \right.$$

$$\left. - \frac{1}{[vd_2(x)^2 + vd_2(y)^2]^{\frac{3}{2}}} \right] p_{B_y}. \quad (34)$$

These are linear equations about the quantities $\mathbf{p}_A$ and $\mathbf{p}_B$ and can be solved numerically. In numerical calculations, an array with the width of 20 nanospheres in the x direction is designed to simulate the one-dimensional nanoribbon. The dipole strengths and the field distribution are plotted in Fig. 6, where two typical polarizations $\theta = 10°$ and $\theta = 120°$ are used. As predicted before, when polarization is $\theta \sim 40°$–$80°$ (or $\sim 100°$–$140°$), there is no edge state, whereas when $\theta \sim 0°$–$20°$ (or $\sim 160°$–$180°$), the edge state appears. The numerical results obviously agree well with the theory.

To testify the robustness of the edge states, random x-direction offsets within $[-5$ nm, $+5$ nm$]$ to the otherwise perfect lattice sites are introduced, as shown in Fig. 7(a). Now that the translation symmetry is broken, we cannot get an eigenequation, but the dipole responses under the perturbation can be numerically solved by the classical method. A finite lattice with a width of 20 nanospheres in the x direction and 40 nanospheres along the y direction is chosen to do the simulation. In Fig. 7(b), the electric field distribution in the nanoribbon is plotted, which clearly shows that the edge state survives after the disorder is introduced.

VI. CONCLUSION

In this study, we investigated the topological physics of a graphene lattice irradiated perpendicularly by a polarized light. Through modeling the photonic system as an eigenproblem and solving it analytically, we showed that the photonic band structure alternately switches from the gapped to gapless structure. Using the Berry phase gathered around the half Brillouin zone as a topological index, we identified the existence of topologically nontrivial states in some of the gapped structures as the polarization angle changes. Our findings reveal the existence of topological nontrivial states in such plasmonic system, and the expected topological phase transition occurs across a range of parameters rather than a single point. We also confirmed the topological nature of the system by examining the edge states in the corresponding lattice nanoribbon. Furthermore, the validity of the theory is also checked by solving the dipole responses through the classical electromagnetic theory; so is the robustness of the edge state under certain lattice disorders. Our results demonstrate the potential for using polarization as a different degree of freedom to control the topological properties in metal nanoparticle lattices, paving the way for multifunctional photonic devices with robust wave control.

ACKNOWLEDGMENT

[1] K. v. Klitzing, G. Dorda, and M. Pepper, Phys. Rev. Lett. **45**, 494 (1980).

[2] M. Z. Hasan and C. L. Kane, Rev. Mod. Phys. **82**, 3045 (2010).

[3] C. L. Kane and E. J. Mele, Phys. Rev. Lett. **95**, 226801 (2005).

[4] T. Ozawa, H. M. Price, A. Amo, N. Goldman, M. Hafezi, L. Lu, M. C. Rechtsman, D. Schuster, J. Simon, O. Zilberberg, and I. Carusotto, Rev. Mod. Phys. **91**, 015006 (2019).

[5] L. Lu, J. D. Joannopoulos, and M. Soljacic, Nat. Photon. **8**, 821 (2014).

[6] A. B. Khanikaev and G. Shvets, Nat. Photon. **11**, 763 (2017).

[7] M. Hafezi, E. A. Demler, M. D. Lukin, and J. M. Taylor, Nat. Phys. **7**, 907 (2011).

[8] B. Bahari, A. Ndao, F. Vallini, A. E. Amili, Y. Fainman, and B. Kante, Science **358**, 636 (2017).

[9] F. D. M. Haldane and S. Raghu, Phys. Rev. Lett. **100**, 013904 (2008).

[10] A. B. Khanikaev, S. H. Mousavi, W. K. Tse, M. Kargarian, A. H. MacDonald, and G. Shvets, Nat. Mater. **12**, 233 (2013).

[11] L.-H. Wu and X. Hu, Phys. Rev. Lett. **114**, 223901 (2015).

[12] W. J. Wang, M. Ramezani, A. I. V. P. Torma, J. G. Rivas, and T. W. Odom, Mater. Today **21**, 303 (2018).

[13] M. Kim and J. Rho, Nanophotonics Berlin **9**, 3227 (2020).

[14] M. Honari-Latifpour and L. Yousefi, Nanophotonics Berlin **8**, 799 (2019).

[15] W. P. Su, J. R. Schrieffer, and A. J. Heeger, Phys. Rev. Lett. **42**, 1698 (1979).

[16] A. Poddubny, A. Miroshnichenko, A. Slobozhanyuk, and Y. Kivshar, ACS Photon. **1**, 101 (2014).

[17] S. Q. Shen, *Topological Insulators Dirac equation in Condensed Matters* (Springer, Berlin, 2012).

[18] C. W. Ling, M. Xiao, C. T. Chan, S. F. Yu, and K. H. Fung, Opt. Express **23**, 2021 (2015).

[19] M.-X. Zhang, Z. Zhou, L. Yan, L. Zhang, and J.-Y. Yan, J. Appl. Phys. **129**, 243103 (2021).

[20] F. Liu, H.-Y. Deng, and K. Wakabayashi, Phys. Rev. B **97**, 035442 (2018).

[21] I. S. Sinev, I. S. Mukhin, A. P. Slobozhanyuk, A. N. Poddubny, A. E. Miroshnichenko, A. K. Samusev, and Y. S. Kivshar, Nanoscale **7**, 11904 (2015).

[22] A. H. Castro Neto, F. Guinea, N. M. R. Peres, K. S. Novoselov, and A. K. Geim, Rev. Mod. Phys. **81**, 109 (2009).

[23] F. J. García de Abajo, Phys. Rev. Lett. **82**, 2776 (1999).

[24] S. Y. Park and D. Stroud, Phys. Rev. B **69**, 125418 (2004).

[25] F. J. García De Abajo, Rev. Mod. Phys. **79**, 1267 (2007).

[26] M. G. Blaber, M. D. Arnold, and M. J. Ford, J. Phys. Chem. C **113**, 3041 (2009).

[27] F. Lemoult, M. F. N. Kaina, and G. Lerosey, Nat. Phys. **9**, 55 (2013).

[28] N. Kaina, F. Lemoult, M. Fink, and G. Lerosey, Appl. Phys. Lett. **102**, 144104 (2013).

[29] F. Liu and K. Wakabayashi, Phys. Rev. Lett. **118**, 076803 (2017).

[30] D. Xiao, M. C. Chang, and Q. Niu, Rev. Mod. Phys. **82**, 1959 (2010).

[31] M. Quinten, A. Leitner, J. R. Krenn, and F. R. Aussenegg, Opt. Lett. **23**, 1331 (1998).

[32] L. Yan, D. Zhang, X.-J. Wang, and J.-Y. Yan, New J. Phys. **25**, 043020 (2023).

[33] D. Zhang, X.-J. Wang, L. Zhang, and J.-Y. Yan, Results Phys. **50**, 106585 (2023).